ACS Catalysis

Research Article

pubs.acs.org/acscatalysis

Reaction Progress Kinetic Analysis as a Tool To Reveal Ligand Effects in Ce(IV)-Driven IrCp*-Catalyzed Water Oxidation

Jacobus M. Koelewijn,[§] Martin Lutz,[#] Wojciech I. Dzik,[§] Remko J. Detz,[§] and Joost N. H. Reek*[,§]

[§]Van 't Hoff Institute for Molecular Sciences, University of Amsterdam, Science Park 904, 1098 XH Amsterdam, Netherlands

[#]Crystal and Structural Chemistry Bijvoet Center for Biomolecular Research, Utrecht University, Padualaan 8, 3584 CH Utrecht, Netherlands

Supporting Information

ABSTRACT: A series of iridium-based complexes have been evaluated in Ce(IV)-driven water oxidation catalysis. Detailed kinetic data have been obtained from UV−vis stopped-flow experiments, and these data have been analyzed using reaction progress kinetic analysis. The graphical plots show that there are three clear phases in the reaction: catalyst activation, water oxidation catalysis, and cerium concentration controlled catalysis at the end of the reaction. The ligand attached to the IrCp* complex has a clear influence on both the activation as well as the catalysis. Some bidentate ligands result in relatively slow catalysis, and the first-order in iridium supports the presence of mononuclear active species; however, other bidentates form the more active dinuclear species. Monodentate ligands allow the formation of *bis-μ-oxo* bridged dimeric species, supported by kinetics displaying 1.6-order in [Ir], leading to high reaction rates.

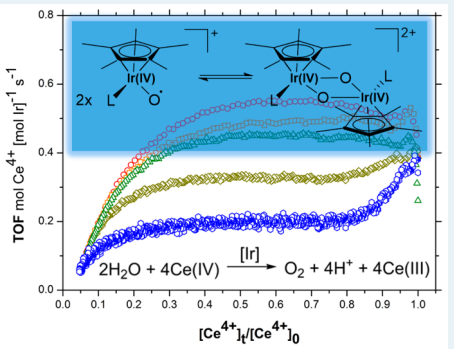

KEYWORDS: *water splitting, homogeneous catalysis, water oxidation, iridium, reaction progress kinetic analysis*

1. INTRODUCTION

The use of energy has played a central part in the advancement of mankind. Since the industrial revolution, the demand for energy has increased rapidly, mostly due to the development of new technologies accompanied by an increase in the global population and increased living standards.[1] Up to now, the majority of this demand has been supplied by the combustion of fossil fuels. However, fossil fuels are limited sources of energy, and more importantly, CO_2 is released upon combustion of fossil fuels, which is undesirable as it is a significant contributor to the greenhouse effect. Of primary concern is that the use of fossil fuels as an energy resource and a chemical feedstock to drive the growing modern economy is unsustainable. A sustainable, carbon neutral, and cost-effective route for the production of fuels to drive the modern economy is one of the biggest current endeavors of mankind. Hydrogen could be considered as an alternative fuel if produced on large scales in a sustainable manner. However, the majority of the production of hydrogen is currently based on the steam reforming of methane and the industrial electrolysis of H_2O using "renewable electricity" is not cost-competitive with the reforming of natural gas. Artificial photosynthesis, a general term that captures all devices that can store solar energy in the form of chemical fuel, for example, hydrogen, by the splitting of H_2O, is recently attracting much attention as this may be an important future solution to this issue.[2,3] The energy output of the sun by far exceeds the current global energy needs, and as such, hydrogen production by making use of the sun's energy and H_2O as a carbon-neutral renewable feedstock is potentially fully sustainable.[4] One approach is to make use of (molecular) catalysts immobilized onto large bandgap semiconductors where H_2O is oxidized at the photoanode ($O_2 + 4H^+ + 4e^- \rightleftharpoons 2H_2O$; $E°$ 1.23 V vs NHE) and protons are reduced at the photocathode ($2H^+ + 2e^- \rightleftharpoons H_2$; $E°$ 0.00 V vs NHE).[5−15] Catalysts able to operate in such an artificial photosynthetic device are essential to ensure a high solar to hydrogen efficiency as they lower the overpotentials required to drive both half-reactions that split water. The water oxidation half-reaction is recognized as a bottleneck in terms of efficient water splitting as it is a kinetically demanding reaction. Slow reaction kinetics on the (photo)anode interface results in high overpotentials needed to drive the oxidation of H_2O at a reasonable rate and, as such, reduces the overall efficiency of solar to hydrogen transformation. The development of novel catalysts that drive the oxidation of H_2O is essential in the development of artificial photosynthetic devices. Factors such as the nature of the catalytically active species that facilitates the oxidation of H_2O, the turn over frequency (TOF in mol O_2 mol cat^{-1} s^{-1}) at which the catalytic cycle is completed, the stability of the catalyst, and the overpotential at which catalysis takes place are crucial to the rational design of devices. Heterogeneous metal oxides based on Ru, Ir, Co, Fe, Ni, and Mn are known to catalyze the oxidation of H_2O where oxides based on iridium often show low overpotentials and high activities.[5,16−25] Molecular transition-metal compounds based on Ru,[26−28] Ir,[29−31] Mn,[32−34] Co,[35−37] and Fe[38−40] among other metals

Received: January 29, 2016
Revised: April 14, 2016

DOI: 10.1021/acscatal.6b00297
ACS Catal. 2016, 6, 3418−3427

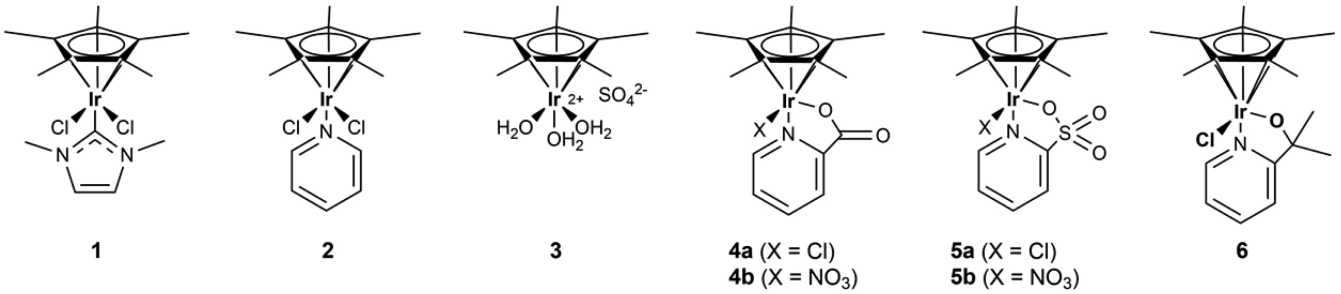

Figure 1. Selected Ir(III)Cp* catalytic precursors used in the Ce(IV)-driven oxidation of H_2O.

are also active for the catalytic oxidation of H_2O, most of them which have recently been reviewed.[41]

Molecular compounds have the advantage that they can be synthetically tailored to optimally match with thermodynamic energy potentials of semiconductors. The interplay between molecular catalysts and photoactivated molecular sensitizers can be studied independently, and information regarding catalytic intermediates, mechanistic pathways, and structural integrity can be studied in a more facile way. Structural integrity of the molecular catalyst is key when strategies involving further functionalization of the molecular complex for electrode surface anchoring or the covalent attachment of molecular sensitizers are considered. In terms of mechanistic insight and the nature of the catalytically active species, ruthenium-based molecular water oxidation catalysts (WOCs) are best understood.[42,43] Mechanistic insight in the operational modes of iridium-based molecular water oxidation catalysis has been proven difficult, and mechanistic studies reported so far are limited.[30,44−48] Since the report of Bernhard, describing the catalytic activity of cyclometalated iridium(III) bis-aqua complexes, molecular water oxidation catalysis based on iridium compounds has gained significant interest.[29] The group of Crabtree reported the catalytic activity of iridium-based half-sandwich complexes of the type IrCp*(N−C)X, IrCp*(N−N)X and [IrCp(N−N)X]X.[30,48] The use of the electron-rich Cp* ligand was a rational design choice as it could stabilize high-valent intermediates during the catalytic oxidation of H_2O.[30] Other groups have reported the activity of various IrCp* compounds with varying bidentate ligands[49−60] among other iridium-based catalytic precursors without Cp*.[61−63] Especially IrCp*$(H_2O)_3$ (complex **3** in Figure 1) shows remarkable catalytic activity.[23,30,50,64−66] All of these reports have in common that the catalysts were studied using either cerium ammonium nitrate (CAN) or sodium periodate ($NaIO_4$) as a sacrificial oxidant with both oxidants having their own advantages and disadvantages.[46,67,68] In some contributions, the degradation of the Cp* ligand has been reported,[69,70] including complete degradation of the catalyst precursor to iridium oxide, although one may argue that this depends on the reaction conditions.[54,71,72]

Apart from being studied using a sacrificial oxidant, iridium WOCs have been studied while covalently bound to other organic moieties,[73−75] integrated into larger molecular architectures like MOFs,[76,77] immobilized onto carbon[78] and ITO[79] based anodes or coimmobilized onto metal oxide substrates with high-valent porphyrin molecular sensitizers.[80,81] However, photodriven oxidation of H_2O using iridium-based catalytic systems has been studied to a limited extend.[82−84]

Our group has reported an active water oxidation catalyst in 2011, in which an N-heterocyclic carbene ligand is bound in a monodentate fashion (Compound **1** in Figure 1).[31] This precursor of the type IrCp*(L)X_2 differs from other reported catalysts as it has two vacant sites at which oxidation of water can occur.[47] The (electro)chemical properties of the hydroxy ligated form of compound **1** (Cl = OH) have been reported and within a certain concentration window, a first-order dependence in CAN and a first-order dependence in catalyst concentration was observed.[31,46] The first-order dependence in the concentration of the catalyst would suggest that the molecular nature of the catalyst remains intact during the oxidation of H_2O. Compound **1**−OH shows a strong pH dependence in electrocatalytic activity, which is in contrast to mesoporous iridium oxide, supporting that for this system the catalytic activity comes from a molecular species.[21,85] With respect to the nature of the catalytically active species, it was reported that under electrocatalytic conditions using complex **1**−OH, using a Au electrode surface and *in situ* Raman spectroscopy, the formation of a *bis-μ-oxo* bridged $[\{Ir^{4+}\}(NHC)Cp^*(\mu\text{-}O)]_2^{2+}$ dimeric species was observed before the onset potential for oxygen formation.[85] Formation of the dimer showed to be reversible upon lowering the anodic potential with the retention of both the Cp* and NHC ligand (Figure 2).[85]

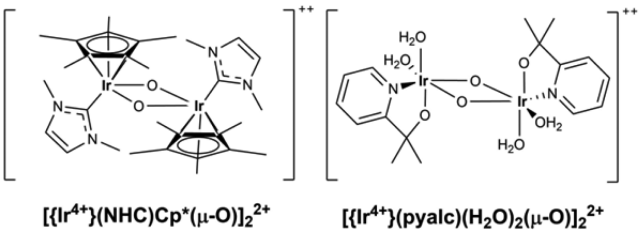

Figure 2. Proposed intermediates in the formation of the catalytically active species for the hydroxy ligated catalytic precursors **1** (left) and **6** (right).[85,86]

The group of Crabtree also has reported evidence for the presence of a *bis-μ-oxo* bridged dimeric iridium species when the hydroxo ligated form of complex **6** (Cl = OH), bearing a 2-(2′-pyridyl)-2-propanolate (pyalc) ligand stable under oxidative conditions, was applied in the catalytic oxidation of H_2O using $NaIO_4$ as the sacrificial oxidant.[65,86−89] It is assumed that this $[\{Ir^{4+}\}(pyalc)(H_2O)_2(\mu\text{-}O)]_2^{2+}$ dimer is the catalyst resting state. In contrast to the former system, the Cp* ligand is removed in the activation process that converts the catalytic precursor to the catalytically active species (Figure 2).[86,88,89] Both authors have reported that after formation of the dimeric species, further oxidation steps of the complex are required before H_2O is catalytically oxidized to O_2.

DOI: 10.1021/acscatal.6b00297
ACS Catal. 2016, 6, 3418−3427

Despite the many reports on IrCp* WOC, a proper comparison of the related but different catalyst systems remains difficult as the catalytic activity is highly dependent on the reaction conditions. Therefore, a proper comparison of reported TOFs and turn over numbers (TONs) is impeded. Apparent ligand effects on the observed catalytic rate, the mechanism, and the formation of the catalytically active species are easily overlooked. In this paper, we demonstrate that the application of reaction progress kinetic analysis (RPKA) on kinetic data, obtained for a selection of IrCp* WOCs (Figure 1), in the CAN-driven catalytic oxidation of H_2O provides new detailed information on the mechanism. The data is obtained using stopped-flow UV−vis spectrometry, which allows rapid mixing of reactive solutions within the millisecond time scale, after which the reaction progress can be monitored by UV−vis. Essential kinetic data at initial reaction is thus obtained, and a full kinetic profile of the catalytic activity can be established. Reaction progress kinetic analysis, a methodology developed by Blackmond,[90] has not been applied to water oxidation catalysis before. We demonstrate in this contribution that the method leads to new insights in the mechanism; specifically, we have further elucidated the influence of the ligand bound to the iridium center on the formation of the catalytically active species in iridium-based water oxidation catalysis.

2. RESULTS AND DISCUSSION

Compounds **1**, **3**, **4a**,**b**, and **6** (Figure 1) were synthesized according to previously published procedures.[31,52,65,91,92] Compound **2** was easily obtained by adding an excess of pyridine to a solution containing $\{IrCp^*Cl_2\}_2$ in CH_2Cl_2, and compound **5a** was prepared by adding NaOMe to a mixture of 2-pyridinesulfonic acid and $\{IrCp^*Cl_2\}_2$ in MeOH. In both procedures, the addition of pentane to the solution results in precipitation of the compound as a yellow amorphous powder in good yield. Compound **5b** was prepared from compound **5a** by exchanging the anion using $AgNO_3$ in CH_2Cl_2 (see Supporting Information for synthetic details). The activity of the various complexes as catalysts in the oxidation of H_2O was determined using CAN as a sacrificial oxidant in 0.1 M HNO_3. The catalytic rate was measured monitoring the decrease in concentration of Ce^{4+} at a wavelength of 360 nm according to reaction eq 1:

$$2H_2O + 4Ce(IV) \xrightarrow{[Ir]} O_2 + 4H^+ + 4Ce(III) \quad (1)$$

The compounds were studied at concentrations ranging from 1 μM to 5 μM in the presence of 1.5 mM CAN. For all measurements, Ce^{4+} was quantitatively consumed. The data obtained for compounds **1**, **2**, and **3** is shown in the top-panels (a−c) of Figure 4. Values for k_{obs} were obtained from the slope of the curves, and an experimentally observed k_{obs} value of 3.52×10^{-8} M s^{-1} was determined as the background reaction (see Figure S4 and S5). It is evident that the obtained kinetic profiles for compound **1**, **2**, and **3** are remarkably similar. For all three compounds, a plot of the observed k_{obs} values against the catalyst concentration immediately reveals similar non first-order behavior in [Ir] (Figure 3a) with an apparent TOF of 0.64−0.73 mol Ce^{4+} [mol Ir]$^{-1}$ s^{-1}.

A conventional log−log plot of k_{obs} against the catalyst concentration reveals an order of 1.6 in [Ir] for all three compounds (Figure 3b). The broken order in the concentration of the catalyst for $[IrCp^*(H_2O)_3]^{2+}$ **3** was previously reported by Crabtree,[30,86] and its unusually high activity

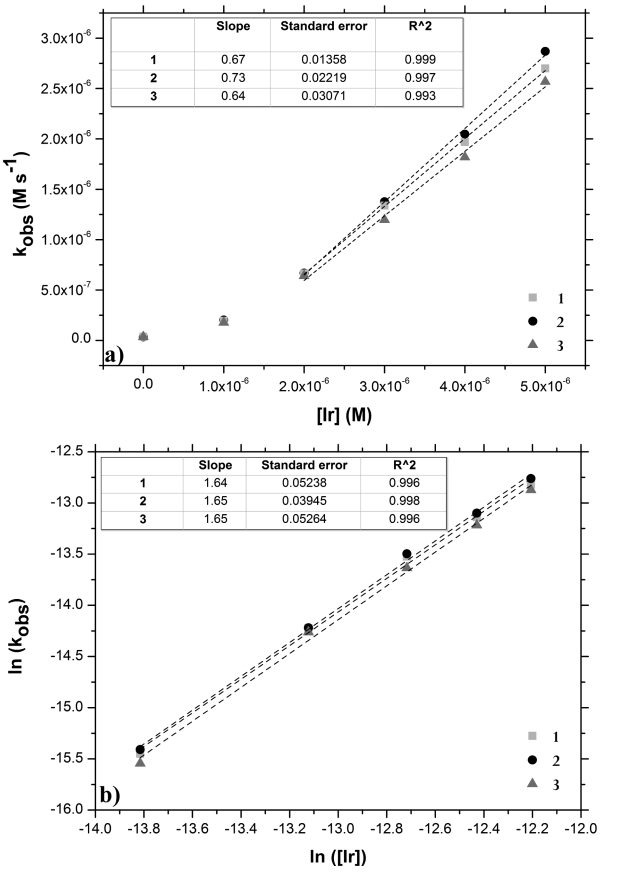

Figure 3. (a) [Ir] plotted against k_{obs} of compounds **1**, **2**, and **3**. The apparent TOF is extracted from the slope using the four highest k_{obs} values. (b) Overlapping respective log−log plots revealing a similar broken order of 1.6 for all three compounds.

compared to bidentate IrCp*(N−C)X precursors was also mentioned by Macchioni (vide infra).[50,59] For IrCp*(NHC)X_2 **1** (X = OH), however, initial studies reported a clear first-order dependence in the concentration of the catalyst when CAN was applied as the chemical oxidant.[31,46] On the basis of the observed broken order in [Ir] found under our experimental conditions for precursor **1** and **2**, this would suggest a rapid loss of the NHC and pyridine ligand, respectively, as well as rapid exchange of the anionic chloride ligands with H_2O, resulting in the in situ formation of $[IrCp^*(H_2O)_3]^{2+}$. This would explain the similarities in the kinetic profile. However, when the same data is represented as a graphical rate equation, distinct changes are observed. In the middle-panels (d−f) of Figure 4, the kinetic data obtained for compound **1**, **2**, and **3** is represented as a graphical rate equation.[90] On the *y*-axis the TOF is plotted, which represents the rate in the Ce^{4+} consumption (in mol Ce^{4+} [mol Ir]$^{-1}$ s^{-1}). On the *x*-axis, the [Ce^{4+}] is plotted, represented as the ratio between the concentration of Ce^{4+} at the start and at time *t* of the reaction. In such a plot, the reaction progress for the consumption of Ce^{4+} should be read starting at the right side of the plot where $[Ce^{4+}]_t/[Ce^{4+}]_0$ equals 1.0. A horizontal trend in the consumption of Ce^{4+} demonstrates a zero-order dependence in [Ce^{4+}], whereas a linear slope progressing toward the origin of the graph points toward an order greater than zero in [Ce^{4+}].[90] In the event that the consumption of Ce^{4+} is first-order dependent in catalyst concentration, and if there is no product inhibition nor catalyst decomposition, the plots of the catalytic reaction performed at

DOI: 10.1021/acscatal.6b00297
ACS Catal. 2016, 6, 3418−3427

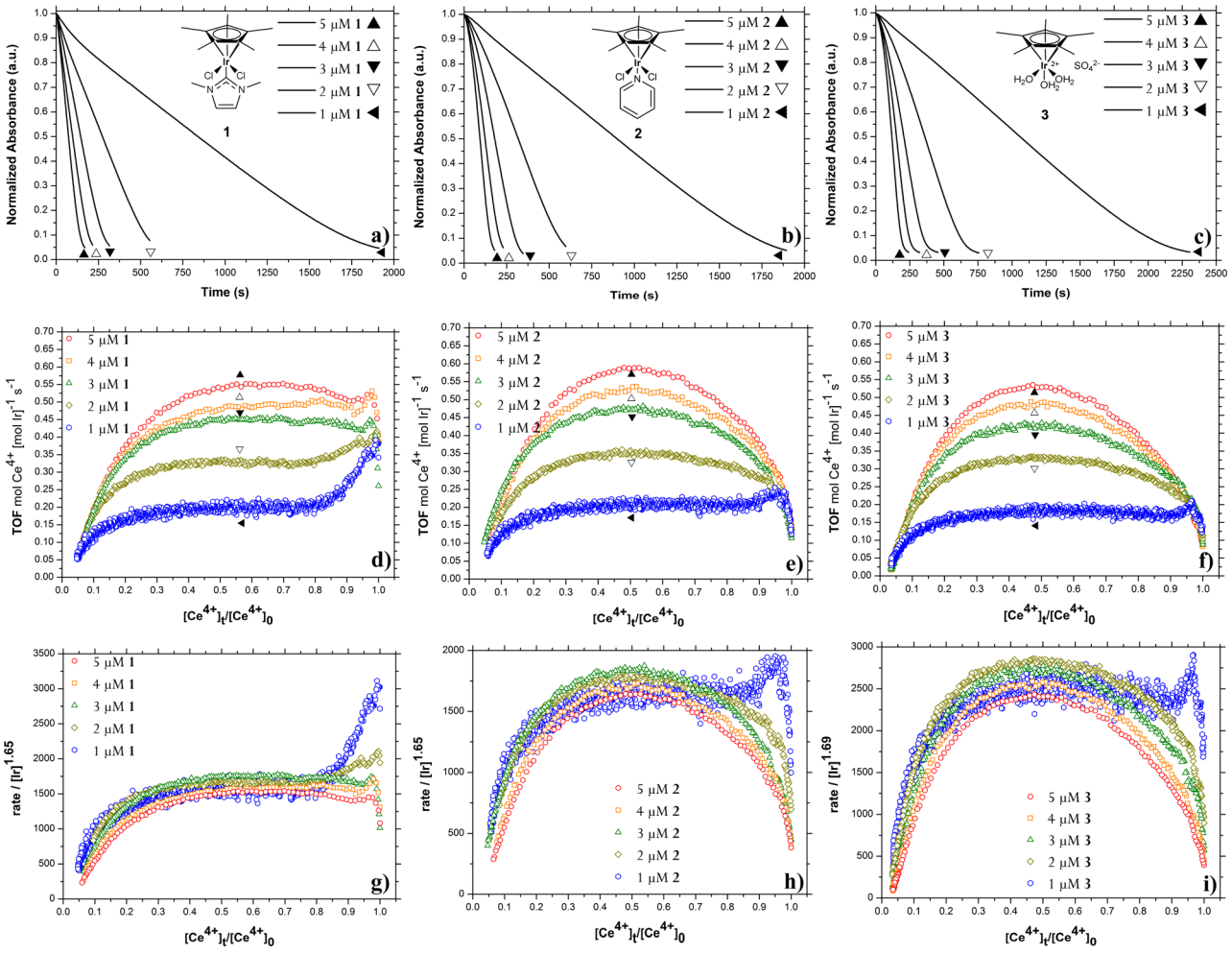

Figure 4. (a,b,c) Kinetic traces for 1−5 μM **1**, **2**, and **3** with 1.5 mM CAN shown in a conventional representation. (d,e,f) Same kinetic data represented as a graphical rate equation. (g,h,i) Same kinetic data represented as rate/$[Ir]^n$ against $[Ce^{4+}]_t/[Ce^{4+}]_0$ where the value of n represents the order of the catalyst.

different catalyst concentrations should overlap.[90] For a non first-order in catalyst concentration, a plot of the rate/$[Ir]^n$ against $[Ce^{4+}]_t/[Ce^{4+}]_o$ where the value of n is found that generates the best overlay of all the curves reflects the order dependence in the catalyst concentration[90] (see Supporting Information for more details). The benefits of using this representation, as opposed to the "classic" representation in the top panels of Figure 4, is the comparison of the entire reaction profile instead of using only a few data points.

For IrCp*(NHC)Cl_2 **1**, (Figure 4d) at catalyst concentrations of 3−5 μM the change in the Ce^{4+} consumption rate seems to occur rapidly, before it reaches a constant value and becomes zero-order dependent in $[Ce^{4+}]$. The consumption rate decreases at the point where the Ce^{4+} concentration is too low and becomes rate limiting. At lower catalyst concentrations, the rate first decreases before it becomes constant and zero-order dependent in $[Ce^{4+}]$. All kinetic curves reveal that after an incubation time a stable catalytically active species is formed which shows a zero-order dependence in Ce^{4+}. A plot of the rate/$[Ir]^n$ against $[Ce^{4+}]/[Ce^{4+}]_0$ was constructed for which it was found that a value of 1.65 for n generates the best overlay of all the curves (Figure 4g).[90] This implies that once the active species has been formed over the full course of the reaction progress, the order of 1.65 is maintained. The graphical rate equations obtained for both IrCp*(pyr)Cl_2 **2** (Figure 4e) and $[IrCp^*(H_2O)_3]^{2+}$ **3** (Figure 4f) show, in contrast to IrCp*(NHC)Cl_2 **1**, that the change in the Ce^{4+} consumption rate occurs gradually, increasing to a maximum value. The rate in Ce^{4+} consumption decreases at the point where $[Ce^{4+}]$ becomes rate limiting, in analogy to what has been described for precursor **1**. In addition, for plots of rate/$[Ir]^n$ against $[Ce^{4+}]/[Ce^{4+}]_0$ a similar order of 1.65 and 1.69 (respectively, Figure 4h,i) was found throughout the course of the reaction progress, which is in good agreement with the order found using the classical approach (Figure 3). The graphical rate equation for IrCp*(pyr)Cl_2 **2** and $[IrCp^*(H_2O)_3]^{2+}$ **3** show a similar trend in the maximum TOF and the reaction order in [Ir]. The graphical rate equation for IrCp*(NHC)Cl_2 **1** is also similar in terms of the maximum TOF and the reaction order in [Ir] but differs in the change of the Ce^{4+} consumption rate at the start of the reaction where $[Ce^{4+}]_t/[Ce^{4+}]_0$ equals 1.0 (highlighted in Figure 5 at 3 μM catalyst concentration and in Figure S8b at 1 μM concentration, indicated by the arrow), which points to a different rate in the formation of the catalytically active species.

In this case, Ce^{4+} is consumed in the process that transforms the catalytic precursor to the catalytically active state and should not be used as a reaction coordinate for the catalytic oxidation of H_2O for reaction progress kinetic analysis; however, within this representation the differences at the initial

DOI: 10.1021/acscatal.6b00297
ACS Catal. 2016, 6, 3418−3427

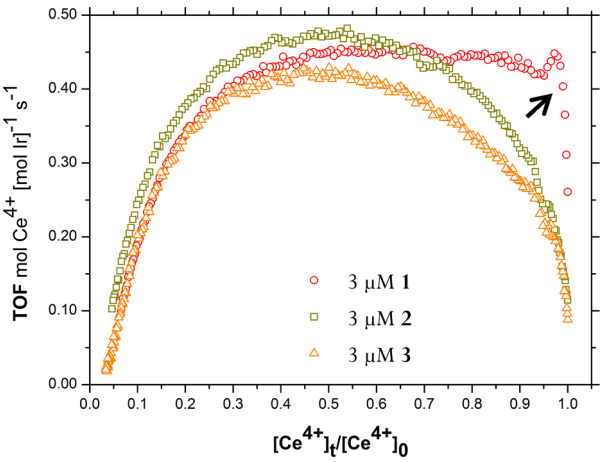

Figure 5. Superposition of the kinetic data represented as a graphical rate equation for IrCp*(NHC)Cl_2 **1**, IrCp*(pyr)Cl_2 **2** and $[IrCp^*(H_2O)_3]^{2+}$ **3** obtained at 3 μM catalyst concentration and 1.5 mM CAN.

phase of the reaction become evident in contrast to the classical representation (Figure 4a–c).

The similarities between IrCp*(pyr)Cl_2 **2** and $[IrCp^*(H_2O)_3]^{2+}$ **3** implies that under the experimental conditions, the pyridine ligand and the chloride anions are readily replaced by H_2O, forming essentially the same catalytic precursor as $[IrCp^*(H_2O)_3]^{2+}$ **3**. The difference in the change of the Ce^{4+} consumption rate for IrCp*(NHC)Cl_2 **1**, however, indicates the influence of the strongly electron-donating NHC ligand. It is assumed that, in contrast to the pyridine ligand, the NHC ligand is retained to the iridium metal center, at least in the initial phase of the reaction, and leads to a more facile oxidation of the metal center and thus to a more rapid formation of the catalytically active species.[47]

When IrCp*(pyalc)Cl **6** is evaluated using the same methodology, a significantly different profile is obtained in terms of the TOF and reaction order in $[Ce^{4+}]$ compared to precursors **1**, **2**, and **3** (Figure 6).

In analogy to the reaction profile of IrCp*(NHC)Cl_2 **1**, it is evident that for IrCp*(pyalc)Cl **6** at catalyst concentrations of 1–5 μM the change in the Ce^{4+} consumption rate occurs rapidly. However, for **6**, the change in the Ce^{4+} consumption rate occurs between a $[Ce^{4+}]_t/[Ce^{4+}]_0$ ratio of 1.0 and 0.90 followed by a decrease in the TOF, showing a clear order

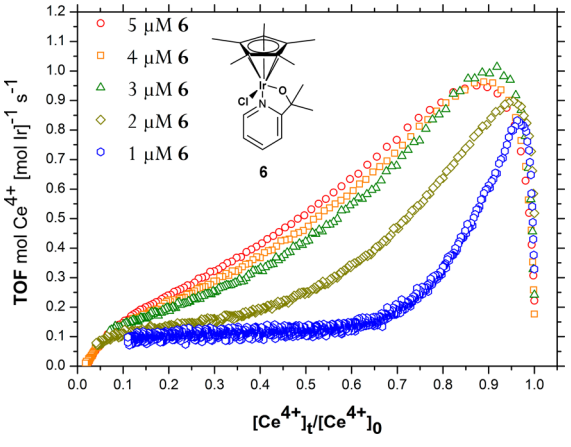

Figure 6. Graphical rate equation for **6** reacting with 1.5 mM CAN.

dependence in $[Ce^{4+}]$ which is greater than zero, whereas for IrCp*(NHC)Cl_2 **1**, the change in the Ce^{4+} consumption rate occurs between a $[Ce^{4+}]_t/[Ce^{4+}]_0$ ratio of 1.0 and 0.97 and follows a clear zero-order until a ratio of 0.5 (Figure 5). This indicates that in the experiment with IrCp*(pyalc)Cl **6**, more Ce^{4+} is consumed during the formation of the active species in comparison to IrCp*(NHC)Cl_2 **1**, and the active species shows a faster rate in the consumption of Ce^{4+} in comparison to the active species formed for IrCp*(NHC)Cl_2 **1**. In addition, the kinetic traces for IrCp*(pyalc)Cl **6** do not overlap in Figure 6, indicating a broken order in the catalyst concentration.

As discussed in the introduction, for the hydroxy ligated IrCp*(NHC)X_2 **1** and IrCp*(pyalc)X **6**, reported by Hetterscheid and Crabtree respectively, evidence was found that under the used experimental conditions the catalytically active species involves a *bis-μ-oxo* bridged dimer (see Figure 2). On the basis of these findings, the trends in the graphical rate equations constructed for compounds **1**, **2**, **3**, and **6** can be explained in two ways: (1) there is a *fast* monomer–dimer equilibrium before the rate-determining step (RDS) of the catalytic reaction that therefore shows up in the overall kinetic equation of the catalytic oxidation of H_2O, in line with which was previously suggested by Crabtree;[30,86] or alternatively, (2) there is a *slow* monomer–dimer equilibrium, and both the dimer and monomer are active in water oxidation. The dimer in this situation displays a higher reaction rate than the monomer, and at higher concentrations, more of the dimer is formed. As both the reaction and the monomer–dimer equilibrium depend on the iridium concentration, the overall [Ir] should be higher than 1. It is likely that the broken order of 1.65 found for IrCp*(NHC)Cl_2 **1** is the result of a similar monomer–dimer equilibrium as found for $[IrCp^*(H_2O)_3]^2$, as displayed also in Figure 7. Oxygen formation is assumed to be facilitated by such

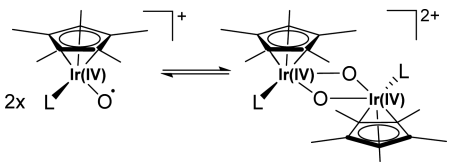

Figure 7. Postulated *bis-μ-oxo* dimer formation in situ for IrCp*(NHC)Cl_2 **1** (L = NHC) and $[IrCp^*(H_2O)_3]^{2+}$ **3** (L = H_2O).

dimers as kinetically faster radical oxo coupling (ROC) pathways become accessible resulting in higher observed TOFs in comparison to monomeric pathways that have to follow a water nucleophilic attack (WNA) mechanism.[93] At higher catalyst concentrations, the equilibrium shifts toward the dimer resulting in a faster observed rate in Ce^{4+} consumption, while at lower catalyst concentrations, the opposite occurs. As the change in the Ce^{4+} consumption rate in the initial phase of the reaction occurs rapidly (Figure 5), it is possible that the NHC ligand is retained upon formation of a catalytically active species of which the molecular structure in solution resembles the dimeric species found for the hydroxo ligated complex **1**–OH when studied under electrocatalytic conditions (Figure 2), where the NHC ligand (L in Figure 7) remains coordinated to the iridium metal.[85]

The graphical rate equation for IrCp*(NHC)Cl_2 **1** in Figure 4d can now be divided into three phases. In the first phase, Ce^{4+} is consumed in the process that transforms the catalytic precursor **1** to the catalytically active species. In the second phase, the observed broken order in iridium is observed, which

DOI: 10.1021/acscatal.6b00297
ACS Catal. 2016, 6, 3418–3427

can be explained as follows: (1) by a catalytic cycle in which a monomer−dimer equilibrium exists within the cycle before the rate-determining step occurs; or alternatively, (2) by two distinct catalytic cycles for both monomeric and dimeric species running in parallel. At higher catalyst concentrations, the ratio of both active species would shift toward the more active dimer resulting in the observation of a faster rate in Ce^{4+} consumption. In the third phase, Ce^{4+} becomes depleted, and the reaction becomes dependent on $[Ce^{4+}]$. For IrCp*(NHC)-Cl_2 **1**, the rate at which the monomer−dimer speciation sets in differs in comparison to IrCp*(pyr)Cl_2 **2** and $[IrCp^*(H_2O)_3]^{2+}$ **3**, due to the electron-donating effect of the NHC ligand. Upon dissolving complex **2**, the pyridine ligand is assumed to be rapidly exchanged with H_2O.

For IrCp*(NHC)Cl_2 **1** the formation of *bis-μ-oxo* bridged species is accessible while the Cp* ligand remains coordinated to the iridium metal due to monodentate nature of the NHC ligand.[47] The bidentate nature of the pyalc ligand in precursor IrCp*(pyalc)Cl **6**, however, initially does not allow the formation of *bis-μ-oxo* bridged species if the Cp* ligand remains attached. For IrCp*(pyalc)Cl **6**, it was reported that the Cp* is indeed lost prior to formation of the active species when $NaIO_4$ is used as the chemical oxidant (Figure 2). This is also supported by the graphical rate equation of compound **6** shown in Figure 6. Prior to formation of the active dimeric $[\{Ir^{4+}\}(pyalc)(H_2O)_2(\mu\text{-}O)]_2^{2+}$ complex, first the Cp* ligand has to be oxidized by Ce^{4+}. This explains the initial higher amount of Ce^{4+} consumption for complex **6** (compared to complex **1**) before a steady-state higher than zero-order dependence in Ce^{4+} is observed. The broken order in the catalyst concentration for IrCp*(pyalc)Cl **6** is explained in analogy to IrCp*(NHC)Cl_2 **1**—that a monomer−dimer equilibrium is established upon formation of the *bis-μ-oxo* bridged dimer and that oxygen formation is facilitated by this dimer resulting in high TOFs. The data suggests that formation of a *bis-μ-oxo* bridged species is a crucial step in the process that converts the catalytic precursor to a rapid catalytically active state.

In order to study the activation processes, experiments with separate solutions of 3 μM catalyst precursor of IrCp*(NHC)-Cl_2 **1** and IrCp*(pyr)Cl_2 **2** were dissolved in 0.1 M HNO_3 and preactivated with 500 equiv of CAN. The solutions where left to stir in the dark for 600 s, such that all Ce^{4+} had reacted, which was visually confirmed by the gradual disappearance of the yellow color of the solution. Injection of the preactivated solutions into the reaction chamber of the stopped-flow spectrophotometer resulted in a final concentration of 3 μM of the respective preactivated catalyst, which was reacted with 1.5 mM CAN in 0.1 M HNO_3 (see Figure S6). Preactivated catalysts should not display an initial incubation phase prior to the second phase in the reaction progress. When the kinetic data for the preactivated IrCp*(pyr)Cl_2 **2** is represented as a graphical rate eq (Figure 8), the trend changes from a parabolic curvature as seen in Figure 4e to a curve showing a zero-order dependence in $[Ce^{4+}]$ after a rapid decrease in the TOF at the initial phase of the reaction. In the initial phase of the reaction, a TOF of ∼0.45 mol Ce^{4+} [mol Ir]$^{-1}$ s^{-1} is observed in line with the maximum TOF of ∼0.45 mol Ce^{4+} [mol Ir]$^{-1}$ s^{-1} observed for both non preactivated catalyst precursors in Figure 4d,e. The rapid decline in TOF leading to a zero-order dependence in Ce^{4+} is attributed to the increased concentration of ammonium nitrate in the reaction solution due to the preactivation step. Coordination of NO_3^- anions to the iridium

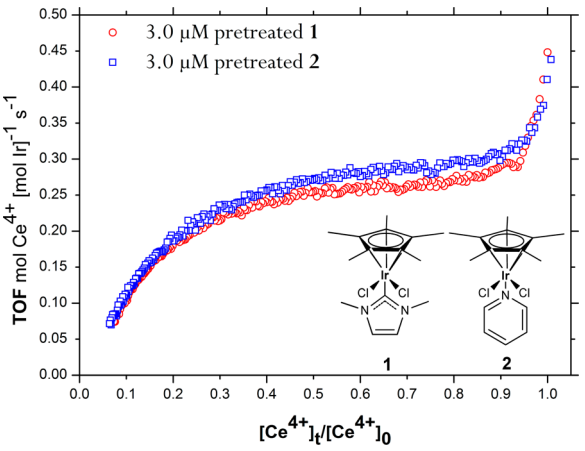

Figure 8. Kinetic data represented as a graphical rate equation for concentrations of 3.0 μM IrCp*(NHC)Cl_2 **1** and IrCp*(pyr)Cl_2 **2** pretreated with 500 equiv of CAN.

center compete with H_2O coordination, which could explain the lower observed TOFs. The graphical rate equation obtained for the preactivated IrCp*(NHC)Cl_2 **1** is similar. The similarities between both curves in Figure 8, suggest that NHC complex **1** and pyridine complex **2** are precursors to a similar active species and that the difference in the Ce^{4+} consumption at the initial phase of the reaction in the absence of preactivation are attributed to the ligands affecting the rate of formation of the active species. The similarities in the TOF for both active species in Figure 8 may suggest that the electron-donating NHC ligand is lost after the incubation process, however, it could also be that the NHC ligand has no direct influence on the rate-determining step of the catalytic cycle for the oxidation of H_2O.

In a study reported by the group of Macchioni, the pyridine carboxylate ligated IrCp*(pyrCO_2)Cl **4a** was evaluated as a WOC using CAN as the chemical oxidant. Under their experimental conditions, a TOF of ∼0.1 mol mol^{-1} s^{-1} was reported for compound **4** with either the chloride (**4a**) or nitrate anion (**4b**) present in the inner coordination sphere.[52] Compared to the apparent TOFs of 0.64−0.73 mol mol^{-1} s^{-1}, found for IrCp*(NHC)Cl_2 **1**, IrCp*(pyr)Cl_2 **2**, and $[IrCp^*(H_2O)_3]^{2+}$ **3**, this is relatively low. This suggests that the bidentate character of the pyridine carboxylate ligand has a large effect in the catalytic oxidation of H_2O. However, the current study shows that IrCp*(pyalc)Cl **6**, of which the 2-(2′-pyridyl)-2-propanolate ligand is also bound in a bidentate fashion, displays a significantly higher TOF of ∼1.0 mol mol^{-1} s^{-1} (Figure 6c). Because of these differences, IrCp*(pyrCO_2)X **4a** and **4b** were reevaluated with the analytical methodology used in this report. In addition, the structurally similar IrCp*(pyrSO_3)X compounds **5a** and **5b**, in which a pyridine sulfonate ligand is bound in a bidentate (κ-N,O) fashion, were evaluated. Pyridine sulfonate ligated IrCp* complexes are so far unexplored systems in the water oxidation reaction. The main question is if these complexes display a similar monomer−dimer equilibrium as observed for **1**, **2**, **3**, and **6**, or if their kinetic profiles show that the mechanism is different. Interestingly, for IrCp*(pyrSO_3)Cl **5a**, a clear broken order of ∼1.6 was found in the catalyst concentration both obtained using the classical approach and by plotting the rate/Ir^n against $[Ce^{4+}]_t/[Ce^{4+}]_0$ (Figure S7a-b and S8a). The broken order indicates that for IrCp*(pyrSO_3)Cl **5a**, a similar monomer−

DOI: 10.1021/acscatal.6b00297
ACS Catal. 2016, 6, 3418−3427

dimer equilibrium is involved. In addition, when compared to the kinetic traces of IrCp*(pyr)Cl_2 **2**, taken at different time resolutions, it becomes evident that both catalysts show the exact same catalytic rate. In addition, the profile at the initial phase of the reaction is the same (Figure S7c and S7d). When a graphical rate equation for the data obtained with IrCp*-($pyrSO_3$)Cl **5a** is constructed, the profile indeed resembles the graphical rate equation observed for IrCp*(pyr)Cl_2 **2** and $[IrCp^*(H_2O)_3]^{2+}$ **3** (Figure 9a).

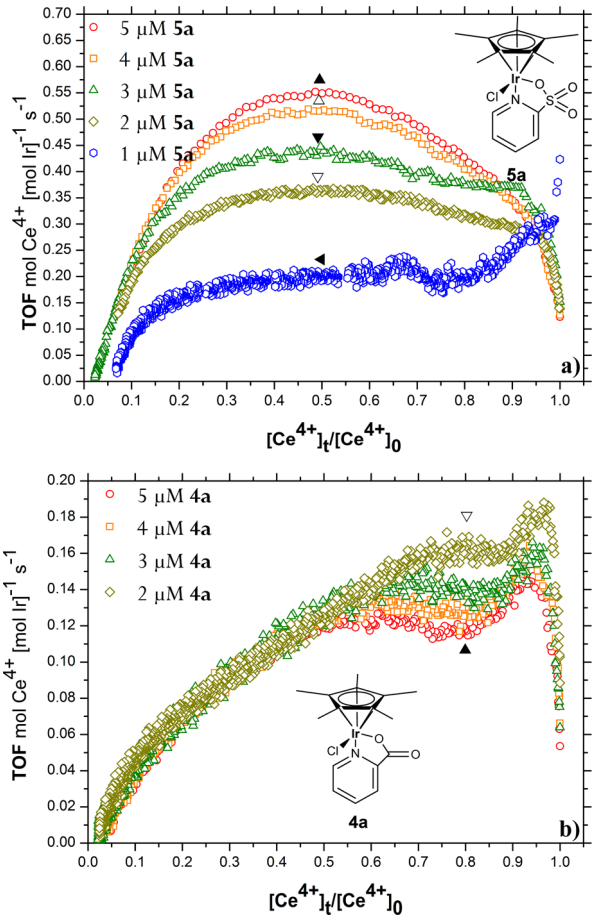

Figure 9. Graphical rate equation for **4a** and **5a** reacting with 1.5 mM CAN.

In contrast, a major difference is observed when a graphical rate equation is constructed for IrCp*($pyrCO_2$)Cl **4a** that was applied under the exact same reaction conditions (Figure 9b). For compound **4a**, the change in the Ce^{4+} consumption rate occurs rapidly at initial reaction conditions; however, a relatively low maximum TOF of 0.18 mol mol^{-1} s^{-1} is obtained, similar to what has been reported by Macchioni.[52] The TOF is a factor three lower as compared to that of IrCp*($pyrSO_3$)Cl **5a**, and a factor six compared to that of IrCp*(pyalc)Cl **6**. The maximum TOF for compound **4a** is followed by a slight decline after which, in the second phase, the Ce^{4+} consumption initially shows a zero-order dependence in $[Ce^{4+}]$. After the second phase, the reaction progress changes and shows a perfect first-order dependence in the catalyst concentration, evident by the overlapping of the curves, and an order dependence higher than zero in $[Ce^{4+}]$ within the region of 0.2−0.5 $[Ce^{4+}]_t/[Ce^{4+}]_0$ evident by the linear progress of the curves to the origin of the graph. Interestingly, in the region in which the system is zero-order in $[Ce^{4+}]$, the TOF is lowest at the highest catalyst concentration (indicated by ▲ in Figure 9b).

The different trends in the graphical rate equations for both compounds can be explained by the coordination strength of the respective ligands. As the graphical rate equation for IrCp*($pyrSO_3$)Cl **5a** resembles the graphical rate equation of IrCp*(pyr)Cl_2 **2** and $[IrCp^*(H_2O)_3]^{2+}$ **3**, the pyridinesulfonate ligand in IrCp*($pyrSO_3$)Cl **5a** presumably also readily dissociates under the acidic experimental conditions like the pyridine ligand in IrCp*(pyr)Cl_2 **2**. In contrast, the pyridinecarboxylate ligand in IrCp*(pyr CO_2)Cl **4a** is retained, affecting the mechanism of the catalytic oxidation of H_2O. Crystallographic data obtained for IrCp*($pyrSO_3$)Cl **5a** and IrCp*($pyrSO_3$)NO_3 **5b** confirm the bidentate character of the ligand in the catalytic precursor as the 2-pyridinesulfonate is ligated in a κ-N,O fashion (Figure 10). The measured Ir1−O1

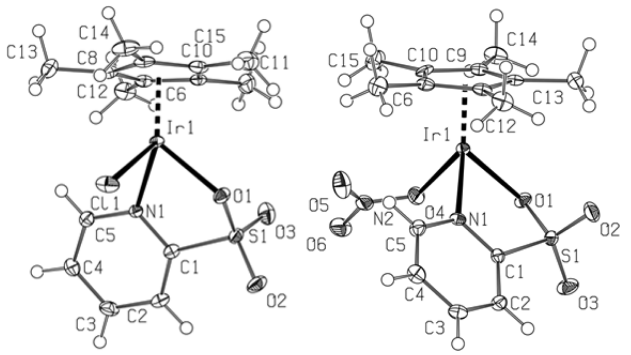

Figure 10. ORTEP representation of IrCp*($pyrSO_3$)Cl **5a** and IrCp*($pyrSO_3$)NO_3 **5b** (ellipsoids at 50% probability level). Selected bond distances for **5a** (Å) Ir1−O1 = 2.177(2), Ir1−N1 = 2.117(3), Ir1−Cl1 = 2.387(10) and **5b** (Å) Ir1−O1 = 2.149(2), Ir1−N1 = 2.135(3), Ir1−O4 = 2.137(2).

bond distances of 2.18 and 2.15 Å found for **5a** and **5b**, respectively, are both slightly longer than the Ir−O bond of 2.10 Å reported for the structurally analogous IrCp*($pyrCO_2$)Cl **4a**. The bond is longer than typical Ir−O bond lengths that range from 2.05 to 2.14 Å.[52,94] The relatively long Ir−O bond length confirms the weak donating properties of the sulfonate anion, in line with the observed facile decoordination under aqueous conditions. In addition, under neutral and acidic conditions, the presence of multiple species are observed when IrCp*($pyrSO_3$)Cl **5a** is dissolved in D_2O, in contrast to IrCp*($pyrCO_2$)Cl **4a** (Figure S9−S12). This means that partial decoordination of the pyridine sulfonate ligand, presumably by decoordination of the sulfonate anion from the iridium center, occurs readily before the catalytic oxidation of H_2O. Effects due to dissociation and oxidation of the chloride ligand by CAN on the catalytic behavior of precursor **4a**, **4b**, **5a**, and **5b** are negligible as no significant differences are observed at initial reaction times (Figure S7e). Also, the trend in Ce^{4+} consumption rate for IrCp*($pyrCO_2$)NO_3 **4b** and IrCp*-($pyrSO_3$)NO_3 **5b** measured at 3 μM catalyst concentration are in line with the observed trends for the respective chloride ligated compounds (Figure S7f). This finding indicates that the chloride and the nitrate anion are readily displaced by H_2O under these experimental conditions.

These observations, in combination with the observed longer Ir−O bond lengths in IrCp*($pyrSO_3$)Cl **5a**, leads to the conclusion that, under catalytic conditions, similar to IrCp*-

DOI: 10.1021/acscatal.6b00297
ACS Catal. 2016, 6, 3418−3427

(pyr)Cl_2 **2**, the pyridine sulfonate ligand dissociates; furthermore, for IrCp*(pyrCO_2)Cl **4a**, the pyridine carboxylate ligand remains attached to the iridium center in a bidentate fashion prior to the catalytic oxidation of H_2O. For IrCp*(pyrCO_2)Cl **4a**, this implies that the precursor is unable to form *bis-μ-oxo* bridged dimeric species during the catalytic oxidation of H_2O. The mechanism for water oxidation is then dominated by kinetically slower WNA pathways rather than faster ROC pathways reflected in the lower observed TOFs and the absence of a broken order in the catalyst concentration for IrCp*(pyrCO_2)Cl **4a**.[93] In the scenario, where the Cp* ligand is detached from IrCp*(pyrCO_2)Cl **4a**, the formation of *bis-μ-oxo* bridged species would become accessible in analogy to the active species of the structurally similar bidentate ligated IrCp*(pyalc)Cl **6**. However, if a monomer−dimer equilibrium would be involved, this should result in a clear broken order in the catalyst concentration of **4a** and therefore at this point is not likely as this is not observed.

The trend in the consumption of Ce^{4+} was compared with the trend in the evolution of O_2 according to eq 1 for compounds **1**, **2**, **3**, **4a**, **5a**, **6**. This was done in an experiment where the O_2 evolution curves were measured in the reaction chamber of a Clark-type electrode by reacting 3 μM of the respective catalyst with 1.5 mM CAN, in accordance with the experimental conditions discussed in this report (see Supporting Information for experimental details). In line with the kinetic experiments, IrCp*(NHC)Cl_2 **1**, IrCp*(pyr)Cl_2 **2**, $[IrCp^*(H_2O)_3]^{2+}$ **3**, and IrCp*(pyrSO_3)Cl **5a** show a similar trend in the rate of O_2 formation in correlation with the similar maximum rate in the consumption of Ce^{4+} observed for these compounds. Both IrCp*(pyrCO_2)Cl **4a** and IrCp*(pyalc)Cl **6** show a different trend. Compound **6** initially shows a more rapid formation of O_2 which gradually declines and compound **4a** shows a slow but steady rate in O_2 formation (Figure 11).

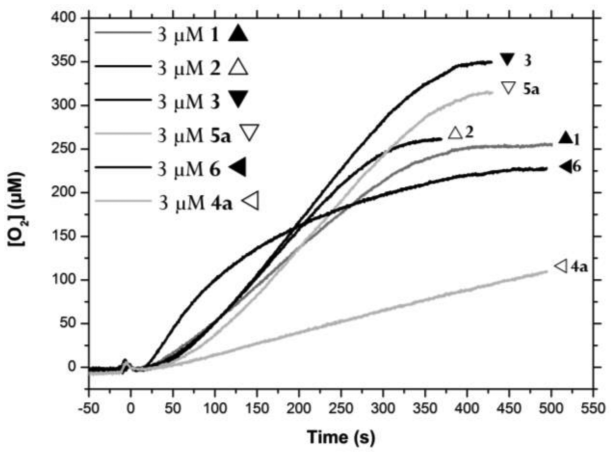

Figure 11. O_2 formation rate for 3 μM [Ir] with 1.5 mM CAN in 0.1 M HNO_3.

For IrCp*(pyrCO_2)Cl **4a**, the slow rate in O_2 formation is in line with the previous made assumption that the catalyst precursor is unable to form *bis-μ-oxo* dimeric species during the catalytic cycle. In Figure S13a−c, the rate in oxygen formation of compounds **1**, **2**, and **6** are compared with the kinetic traces of the rate in Ce^{4+} consumption; however, on the basis of the Clark-electrode data, a difference in the onset of O_2 formation for IrCp*(NHC)Cl_2 **1**, due to faster activation of the catalyst and formation of a monomer−dimer equilibrium which is evident on the basis of the graphical rate equation, could not be observed.

Absorption changes in the region of 450−650 nm have previously been ascribed to the formation of catalytically active species for related IrCp* complexes during the catalytic oxidation of H_2O.[71,86] In addition to the kinetic profiles obtained for **1**, **2**, **3**, **4a**, and **6** by tracing the changes in the UV−vis absorbance intensity related to the decrease in $[Ce^{4+}]$, the increase in absorption intensity in the 450−650 nm region was also studied under millisecond stopped-flow conditions. In these experiments, the catalyst and CAN concentration was increased by a factor 30 with respect to the kinetic experiments to allow the detection of the catalytic species, yet the ratio between the oxidant and the catalyst remained the same (see Figure S14−S17). The UV−vis measurements show that for the different iridium complexes, different catalytic species are formed. However, at these higher catalyst concentrations, there is no evidence for a more rapid formation of the catalytically active species when IrCp*(NHC)Cl_2 **1** is used, in comparison to IrCp*(pyr)Cl_2 **2** and $[IrCp^*(H_2O)_3]^{2+}$ **3**. At higher catalyst concentrations, partly oxidized iridium species formed during the catalytic cycle are more prone to cluster to form larger particles.[72] For this reason, the gradual increase in the absorbance intensity observed for IrCp*(NHC)Cl_2 **1**, IrCp*(pyr)Cl_2 **2**, and $[IrCp^*(H_2O)_3]^{2+}$ **3** (Figure S17a) could be ascribed to catalyst activation (and possibly also decomposition) processes resulting in a mixtures of species. IrCp*(pyalc)Cl **6** and IrCp*(pyr CO_2)Cl **4a** do not show a gradual increase in the absorbance intensity (Figure S16) suggesting that the bidentate nature of the ligand results in more stable catalytically active species at these higher catalyst concentrations. Remarkably, it seems that similar concentrations of a catalytically active species are formed, yet as demonstrated earlier, the TOF with respect to the oxidation of H_2O is significantly higher for the active species formed from precursor **6** than that formed from precursor **4a**, as indicated by both the consumption of Ce^{4+} as well as the formation of O_2. This is mainly attributed to the accessibility of precursor **6** to form *bis-μ-oxo* bridged species in the process that converts the precursor to the active species in contrast to precursor **4**. This highlights that a minor change in the ligand structure leads to a large change in the observed catalytic activity, which clearly points to the involvement of the ligand in the formation of the catalytically active species.

CONCLUSION

The application of reaction progress kinetic analysis based on kinetic data obtained with stopped-flow UV−vis spectroscopy, reveals ligand effects when IrCp* complexes are applied at low catalyst concentrations in the Ce^{4+} driven oxidation of H_2O. The methodology allows the observation of changes in the Ce^{4+} consumption rate, which normally would have been overseen. Instead of assuming a fixed order in $[Ce^{4+}]$, as is generally reported in the literature, it is clearly evident that the consumption rate and order in $[Ce^{4+}]$ differ throughout the course of the reaction yielding information about the influence of the ligand environment on the formation of the catalytically active species. The current study shows that the ligand environment of IrCp* catalytic precursors determines if the formation of *bis-μ-oxo* bridged species, leading to fast catalytically active species, is accessible. The formation of the catalytically active species and the influence of the ligand structure is dependent on the concentration of the catalytic

DOI: 10.1021/acscatal.6b00297
ACS Catal. 2016, 6, 3418−3427

precursor. At higher catalyst concentrations, the results suggest that catalyst precursors with ligands bound in a bidentate fashion are less prone to decomposition reactions compared to catalyst precursors with ligands bound in a monodentate fashion. However, at lower catalyst concentrations, strongly coordinating bidentate ligands hamper the formation of *bis-μ-oxo* bridged species if the Cp* ligand remains attached to the iridium metal as evident for the pyridine carboxylate catalytic precursor **4a**. At higher catalyst concentrations, catalyst precursor **1** with the NHC ligand bound in a monodentate fashion is more prone to decomposition reactions; however, at lower catalyst concentrations, the monodentate nature of the ligand allows for the formation of *bis-μ-oxo* bridged dimers, which the N-heterocyclic ligand displays a role in the rate in formation of the catalytically active species, at least in the beginning of the reaction. On the basis of the results obtained with this methodology, it is concluded that with respect to iridium-based molecular water oxidation catalysts, the formation of *bis-μ-oxo* bridged species is a crucial step in the transformation of the catalytic precursor to a catalytically active state that shows high TOFs with respect to the catalytic oxidation of H_2O. It is assumed that the formation of such species facilitates the formation of oxygen through a kinetically faster (radical) pathway.

■ ASSOCIATED CONTENT

Supporting Information

The Supporting Information is available free of charge on the ACS Publications website at DOI: 10.1021/acscatal.6b00297.

Additional data (Figures S1−S17) as noted in the text (PDF)

X-ray data (CIF)

X-ray data (CIF)

■ AUTHOR INFORMATION

Corresponding Author

*E-mail: j.n.h.reek@uva.nl.

Notes

The authors declare no competing financial interest.

■ ACKNOWLEDGMENTS

This work was carried out within the research programme of BioSolar Cells, cofinanced by the Dutch Ministry of Economic Affairs.

■ REFERENCES

(1) Lewis, N. S.; Nocera, D. G. *Proc. Natl. Acad. Sci. U. S. A.* **2006**, *103*, 15729−15735.

(2) Barber, J. *Chem. Soc. Rev.* **2009**, *38*, 185−196.

(3) Kärkäs, M. D.; Johnston, E. V.; Verho, O.; Akermark, B. *Acc. Chem. Res.* **2014**, *47*, 100−111.

(4) Contreras, M. A.; Deb, S. In *Fundamentals of materials for energy and environmental sustainability*, Ginley, D. S., Cahen, D.; Eds.; Cambridge University Press: Cambridge, U.K., 2012; pp 206−215.

(5) Youngblood, J. W.; Lee, S. H. A.; Kobayashi, Y.; Hernandez-Pagan, E. A.; Hoertz, P. G.; Moore, T. A.; Moore, A. L.; Gust, D.; Mallouk, T. E. *J. Am. Chem. Soc.* **2009**, *131*, 926−927.

(6) Li, L.; Duan, L.; Xu, Y.; Gorlov, M.; Hagfeldt, A.; Sun, L. *Chem. Commun.* **2010**, *46*, 7307.

(7) Brimblecombe, R.; Koo, A.; Dismukes, G. C.; Swiegers, G. F.; Spiccia, L. *J. Am. Chem. Soc.* **2010**, *132*, 2892−2894.

(8) Reece, S. Y.; Hamel, J. A.; Sung, K.; Jarvi, T. D.; Esswein, A. J.; Pijpers, J. J. H.; Nocera, D. G. *Science* **2011**, *334*, 645−648.

(9) Zhao, Y.; Swierk, J. R.; Megiatto, J. D.; Sherman, B.; Youngblood, W. J.; Qin, D.; et al. *Proc. Natl. Acad. Sci. U. S. A.* **2012**, *109*, 15612−15616.

(10) Abdi, F. F.; Han, L.; Smets, A. H. M.; Zeman, M.; Dam, B.; van de Krol, R. *Nat. Commun.* **2013**, *4*, 1−7.

(11) Gao, Y.; Ding, X.; Liu, J.; Wang, L.; Lu, Z.; Li, L.; Sun, L. *J. Am. Chem. Soc.* **2013**, *135*, 4219−4222.

(12) Ji, Z.; He, M.; Huang, Z.; Ozkan, U.; Wu, Y. *J. Am. Chem. Soc.* **2013**, *135*, 11696−11699.

(13) Zhang, L.; Gao, Y.; Ding, X.; Yu, Z.; Sun, L. *ChemSusChem* **2014**, *7*, 2801−2804.

(14) Fan, K.; Li, F.; Wang, L.; Daniel, Q.; Gabrielsson, E.; Sun, L. *Phys. Chem. Chem. Phys.* **2014**, *16*, 25234−25240.

(15) Klepser, B. M.; Bartlett, B. M. *J. Am. Chem. Soc.* **2014**, *136*, 1694−1697.

(16) Kuwabara, T.; Tomita, E.; Sakita, S.; Hasegawa, D.; Sone, K.; Yagi, M. *J. Phys. Chem. C* **2008**, *112*, 3774−3779.

(17) Yagi, M.; Tomita, E.; Sakita, S.; Kuwabara, T.; Nagai, K. *J. Phys. Chem. B* **2005**, *109*, 21489−21491.

(18) Harriman, A.; Pickering, I. J.; Thomas, J. M.; Christensen, P. A. *J. Chem. Soc., Faraday Trans. 1* **1988**, *84*, 2795−2806.

(19) Hoertz, P. G.; Kim, Y. I.; Youngblood, W. J.; Mallouk, T. E. *J. Phys. Chem. B* **2007**, *111*, 6845−6856.

(20) Morris, N. D.; Suzuki, M.; Mallouk, T. E. *J. Phys. Chem. A* **2004**, *108*, 9115−9119.

(21) Nakagawa, T.; Beasley, C. a.; Murray, R. W. *J. Phys. Chem. C* **2009**, *113*, 12958−12961.

(22) Zhao, Y.; Vargas-Barbosa, N. M.; Hernandez-Pagan, E. A.; Mallouk, T. E. *Small* **2011**, *7*, 2087−2093.

(23) Blakemore, J. D.; Mara, M. W.; Kushner-Lenhoff, M. N.; Schley, N. D.; Konezny, S. J.; Rivalta, I.; Negre, C. F. A.; Snoeberger, R. C.; Kokhan, O.; Huang, J.; Stickrath, A.; Tran, L. A.; Parr, M. L.; Chen, L. X.; Tiede, D. M.; Batista, V. S.; Crabtree, R. H.; Brudvig, G. W. *Inorg. Chem.* **2013**, *52*, 1860−1871.

(24) Kanan, M. W.; Nocera, D. G. *Science* **2008**, *321*, 1072−1075.

(25) Mamaca, N.; Mayousse, E.; Arrii-Clacens, S.; Napporn, T. W.; Servat, K.; Guillet, N.; Kokoh, K. B. *Appl. Catal., B* **2012**, *111−112*, 376−380.

(26) Gersten, S. W.; Samuels, G. J.; Meyer, T. J. *J. Am. Chem. Soc.* **1982**, *104*, 4029−4030.

(27) Concepcion, J. J.; Jurss, J. W.; Templeton, J. L.; Meyer, T. J. *J. Am. Chem. Soc.* **2008**, *130*, 16462−16463.

(28) Duan, L.; Bozoglian, F.; Mandal, S.; Stewart, B.; Privalov, T.; Llobet, A.; Sun, L. *Nat. Chem.* **2012**, *4*, 418−423.

(29) McDaniel, N. D.; Coughlin, F. J.; Tinker, L. L.; Bernhard, S. *J. Am. Chem. Soc.* **2008**, *130*, 210−217.

(30) Blakemore, J. D.; Schley, N. D.; Balcells, D.; Hull, J. F.; Olack, G. W.; Incarvito, C. D.; Eisenstein, O.; Brudvig, G. W.; Crabtree, R. H. *J. Am. Chem. Soc.* **2010**, *132*, 16017−16029.

(31) Hetterscheid, D. G. H.; Reek, J. N. H. *Chem. Commun.* **2011**, *47*, 2712.

(32) Limburg, J.; Vrettos, J. S.; Liable-Sands, L. M.; Rheingold, a L.; Crabtree, R. H.; Brudvig, G. W. *Science* **1999**, *283*, 1524−1527.

(33) Berggren, G.; Thapper, A.; Huang, P.; Eriksson, L.; Styring, S.; Anderlund, M. F. *Inorg. Chem.* **2011**, *50*, 3425−3430.

(34) Young, K. J.; Takase, M. K.; Brudvig, G. W. *Inorg. Chem.* **2013**, *52*, 7615−7622.

(35) Dogutan, D. K.; McGuire, R.; Nocera, D. G. *J. Am. Chem. Soc.* **2011**, *133*, 9178−9180.

(36) Huang, Z.; Luo, Z.; Geletii, Y. V.; Vickers, J. W.; Yin, Q.; Wu, D.; Hou, Y.; Ding, Y.; Song, J.; Musaev, D. G.; Hill, C. L.; Lian, T. *J. Am. Chem. Soc.* **2011**, *133*, 2068−2071.

(37) Abe, T.; Nagai, K.; Kabutomori, S.; Kaneko, M.; Tajiri, A.; Norimatsu, T. *Angew. Chem., Int. Ed.* **2006**, *45*, 2778−2781.

(38) Parent, A. R.; Nakazono, T.; Lin, S.; Utsunomiya, S.; Sakai, K. *Dalton Trans.* **2014**, *43*, 12501−12513.

(39) Zhang, B.; Li, F.; Yu, F.; Cui, H.; Zhou, X.; Li, H.; Wang, Y.; Sun, L. *Chem. - Asian J.* **2014**, *9*, 1515−1518.

DOI: 10.1021/acscatal.6b00297
ACS Catal. 2016, 6, 3418−3427

(40) Fillol, J. L.; Codolà, Z.; Garcia-Bosch, I.; Gómez, L.; Pla, J. J.; Costas, M. *Nat. Chem.* **2011**, *3*, 807−813.
(41) Blakemore, J. D.; Crabtree, R. H.; Brudvig, G. W. *Chem. Rev.* **2015**, *115*, 12974−13005.
(42) Gagliardi, C. J.; Vannucci, A. K.; Concepcion, J. J.; Chen, Z.; Meyer, T. J. *Energy Environ. Sci.* **2012**, *5*, 7704.
(43) Sala, X.; Maji, S.; Bofill, R.; García-Antón, J.; Escriche, L.; Llobet, A. *Acc. Chem. Res.* **2014**, *47*, 504−516.
(44) Poater, A.; Ragone, F.; Correa, A.; Cavallo, L. *Dalt. Trans.* **2011**, *40*, 11066.
(45) Liao, R.-Z.; Siegbahn, P. E. M. *ACS Catal.* **2014**, *4*, 3937−3949.
(46) Hetterscheid, D. G. H.; Reek, J. N. H. *Eur. J. Inorg. Chem.* **2014**, *2014*, 742−749.
(47) Venturini, A.; Barbieri, A.; Reek, J. N. H.; Hetterscheid, D. G. H. *Chem. - Eur. J.* **2014**, *20*, 5358−5368.
(48) Hull, J. F.; Balcells, D.; Blakemore, J. D.; Incarvito, C. D.; Eisenstein, O.; Brudvig, G. W.; Crabtree, R. H. *J. Am. Chem. Soc.* **2009**, *131*, 8730−8731.
(49) Lalrempuia, R.; McDaniel, N. D.; Müller-Bunz, H.; Bernhard, S.; Albrecht, M. *Angew. Chem., Int. Ed.* **2010**, *49*, 9765−9768.
(50) Savini, A.; Bellachioma, G.; Ciancaleoni, G.; Zuccaccia, C.; Zuccaccia, D.; Macchioni, A. *Chem. Commun.* **2010**, *46*, 9218.
(51) Brewster, T. P.; Blakemore, J. D.; Schley, N. D.; Incarvito, C. D.; Hazari, N.; Brudvig, G. W.; Crabtree, R. H. *Organometallics* **2011**, *30*, 965−973.
(52) Bucci, A.; Savini, A.; Rocchigiani, L.; Zuccaccia, C.; Rizzato, S.; Albinati, A.; Llobet, A.; Macchioni, A. *Organometallics* **2012**, *31*, 8071−8074.
(53) Hong, D.; Murakami, M.; Yamada, Y.; Fukuzumi, S. *Energy Environ. Sci.* **2012**, *5*, 5708−5716.
(54) Junge, H.; Marquet, N.; Kammer, A.; Denurra, S.; Bauer, M.; Wohlrab, S.; Gärtner, F.; Pohl, M.-M.; Spannenberg, A.; Gladiali, S.; Beller, M. *Chem. - Eur. J.* **2012**, *18*, 12749−12758.
(55) Codolà, Z.; Cardoso, J. M. S.; Royo, B.; Costas, M.; Lloret-Fillol, J. *Chem. - Eur. J.* **2013**, *19*, 7203−7213.
(56) Lewandowska-Andralojc, A.; Polyansky, D. E.; Wang, C.-H.; Wang, W.-H.; Himeda, Y.; Fujita, E. *Phys. Chem. Chem. Phys.* **2014**, *16*, 11976.
(57) Savini, A.; Bucci, A.; Bellachioma, G.; Giancola, S.; Palomba, F.; Rocchigiani, L.; Rossi, A.; Suriani, M.; Zuccaccia, C.; Macchioni, A. *J. Organomet. Chem.* **2014**, *771*, 24−32.
(58) Depasquale, J.; Nieto, I.; Reuther, L. E.; Herbst-Gervasoni, C. J.; Paul, J. J.; Mochalin, V.; Zeller, M.; Thomas, C. M.; Addison, A. W.; Papish, E. T. *Inorg. Chem.* **2013**, *52*, 9175−9183.
(59) Savini, A.; Bucci, A.; Bellachioma, G.; Rocchigiani, L.; Zuccaccia, C.; Llobet, A.; Macchioni, A. *Eur. J. Inorg. Chem.* **2014**, *2014*, 690−697.
(60) Zhang, T.; Dekrafft, K. E.; Wang, J. L.; Wang, C.; Lin, W. *Eur. J. Inorg. Chem.* **2014**, *2014*, 698−707.
(61) Dzik, W. I.; Calvo, S. E.; Reek, J. N. H.; Lutz, M.; Ciriano, M. A.; Tejel, C.; Hetterscheid, D. G. H.; de Bruin, B. *Organometallics* **2011**, *30*, 372−374.
(62) Parent, A. R.; Blakemore, J. D.; Brudvig, G. W.; Crabtree, R. H. *Chem. Commun.* **2011**, *47*, 11745.
(63) Savini, A.; Bellachioma, G.; Bolaño, S.; Rocchigiani, L.; Zuccaccia, C.; Zuccaccia, D.; Macchioni, A. *ChemSusChem* **2012**, *5*, 1415−1419.
(64) Blakemore, J. D.; Schley, N. D.; Olack, G. W.; Incarvito, C. D.; Brudvig, G. W.; Crabtree, R. H. *Chem. Sci.* **2011**, *2*, 94.
(65) Schley, N. D.; Blakemore, J. D.; Subbaiyan, N. K.; Incarvito, C. D.; D'Souza, F.; Crabtree, R. H.; Brudvig, G. W. *J. Am. Chem. Soc.* **2011**, *133*, 10473−10481.
(66) Blakemore, J. D. J.; Schley, N. D.; Kushner-Lenhoff, M. N.; Winter, A. M.; D'Souza, F.; Crabtree, R. H.; Brudvig, G. W. *Inorg. Chem.* **2012**, *51*, 7749−7763.
(67) Wasylenko, D. J.; Ganesamoorthy, C.; Henderson, M. a.; Berlinguette, C. P. *Inorg. Chem.* **2011**, *50*, 3662−3672.
(68) Pecht, I.; Luz, Z. *J. Am. Chem. Soc.* **1965**, *87*, 4068−4072.
(69) Savini, A.; Belanzoni, P.; Bellachioma, G.; Zuccaccia, C.; Zuccaccia, D.; Macchioni, A. *Green Chem.* **2011**, *13*, 3360.
(70) Zuccaccia, C.; Bellachioma, G.; Bortolini, O.; Bucci, A.; Savini, A.; Macchioni, A. *Chem. - Eur. J.* **2014**, *20*, 3446−3456.
(71) Grotjahn, D. B.; Brown, D. B.; Martin, J. K.; Marelius, D. C.; Abadjian, M.-C.; Tran, H. N.; Kalyuzhny, G.; Vecchio, K. S.; Specht, Z. G.; Cortes-Llamas, S. A.; Miranda-Soto, V.; van Niekerk, C.; Moore, C. E.; Rheingold, A. L. *J. Am. Chem. Soc.* **2011**, *133*, 19024−19027.
(72) Hintermair, U.; Hashmi, S. M.; Elimelech, M.; Crabtree, R. H. *J. Am. Chem. Soc.* **2012**, *134*, 9785−9795.
(73) Vagnini, M. T.; Smeigh, A. L.; Blakemore, J. D.; Eaton, S. W.; Schley, N. D.; D'Souza, F.; Crabtree, R. H.; Brudvig, G. W.; Co, D. T.; Wasielewski, M. R. *Proc. Natl. Acad. Sci. U. S. A.* **2012**, *109*, 15651−15656.
(74) Vagnini, M. T.; Mara, M. W.; Harpham, M. R.; Huang, J.; Shelby, M. L.; Chen, L. X.; Wasielewski, M. R. *Chem. Sci.* **2013**, *4*, 3863.
(75) Gupta, S. K.; Choudhury, J. *Dalt. Trans.* **2015**, *44*, 1233−1239.
(76) Wang, C.; Xie, Z.; DeKrafft, K. E.; Lin, W. *J. Am. Chem. Soc.* **2011**, *133*, 13445−13454.
(77) Wang, C.; Wang, J.; Lin, W. *J. Am. Chem. Soc.* **2012**, *134*, 19895−19908.
(78) deKrafft, K. E.; Wang, C.; Xie, Z.; Su, X.; Hinds, B. J.; Lin, W. *ACS Appl. Mater. Interfaces* **2012**, *4*, 608−613.
(79) Joya, K. S.; Subbaiyan, N. K.; D'Souza, F. D.; de Groot, H. J. M. *Angew. Chem., Int. Ed.* **2012**, *51*, 9601−9605.
(80) Moore, G. F.; Blakemore, J. D.; Milot, R. L.; Hull, J. F.; Song, H.; Cai, L.; Schmuttenmaer, C. a.; Crabtree, R. H.; Brudvig, G. W. *Energy Environ. Sci.* **2011**, *4*, 2389.
(81) Poddutoori, P. K.; Thomsen, J. M.; Milot, R. L.; Sheehan, S. W.; Negre, C. F. A.; Garapati, V. K. R.; Schmuttenmaer, C. A.; Batista, V. S.; Brudvig, G. W.; van der Est, A. *J. Mater. Chem. A* **2015**, *3*, 3868−3879.
(82) Petronilho, A.; Rahman, M.; Woods, J. A.; Al-Sayyed, H.; Müller-Bunz, H.; Don MacElroy, J. M.; Bernhard, S.; Albrecht, M. *Dalton Trans.* **2012**, *41*, 13074−13080.
(83) Badia-Bou, L.; Mas-Marza, E.; Rodenas, P.; Barea, E. M.; Fabregat-Santiago, F.; Gimenez, S.; Peris, E.; Bisquert, J. *J. Phys. Chem. C* **2013**, *117*, 3826−3833.
(84) Chen, H.-C.; Hetterscheid, D. G. H.; Williams, R. M.; van der Vlugt, J. I.; Reek, J. N. H.; Brouwer, A. M. *Energy Environ. Sci.* **2015**, *8*, 975−982.
(85) Diaz-Morales, O.; Hersbach, T. J. P.; Hetterscheid, D. G. H.; Reek, J. N. H.; Koper, M. T. M. *J. Am. Chem. Soc.* **2014**, *136*, 10432−10439.
(86) Hintermair, U.; Sheehan, S. W.; Parent, A. R.; Ess, D. H.; Richens, D. T.; Vaccaro, P. H.; Brudvig, G. W.; Crabtree, R. H. *J. Am. Chem. Soc.* **2013**, *135*, 10837−10851.
(87) Ingram, A. J.; Wolk, A. B.; Flender, C.; Zhang, J.; Johnson, C. J.; Hintermair, U.; Crabtree, R. H.; Johnson, M. A.; Zare, R. N. *Inorg. Chem.* **2014**, *53*, 423−433.
(88) Thomsen, J. M.; Sheehan, S. W.; Hashmi, S. M.; Campos, J.; Hintermair, U.; Crabtree, R. H.; Brudvig, G. W. *J. Am. Chem. Soc.* **2014**, *136*, 13826−13834.
(89) Sheehan, S. W.; Thomsen, J. M.; Hintermair, U.; Crabtree, R. H.; Brudvig, G. W.; Schmuttenmaer, C. A. *Nat. Commun.* **2015**, *6*, 6469.
(90) Blackmond, D. G. *Angew. Chem., Int. Ed.* **2005**, *44*, 4302−4320.
(91) Ogo, S.; Makihara, N.; Watanabe, Y. *Organometallics* **1999**, *18*, 5470−5474.
(92) Xiao, X.-Q.; Jin, G.-X. *J. Organomet. Chem.* **2008**, *693*, 3363−3368.
(93) Graeupner, J.; Hintermair, U.; Huang, D. L.; Thomsen, J. M.; Takase, M.; Campos, J.; Hashmi, S. M.; Elimelech, M.; Brudvig, G. W.; Crabtree, R. H. *Organometallics* **2013**, *32*, 5384−5390.
(94) Gorol, M.; Roesky, H. W.; Noltemeyer, M.; Schmidt, H. G. *Eur. J. Inorg. Chem.* **2005**, *2005*, 4840−4844.

DOI: 10.1021/acscatal.6b00297
ACS Catal. 2016, 6, 3418−3427